coatings

MDPI

*Article*

# Spray Parameters and Coating Microstructure Relationship in Suspension Plasma Spray $TiO_2$ Coatings

**Garima Mittal [1], Nigar Gul Malik [1], Arunima Bhuvanendran Nair Jayakumari [1], David Martelo [2], Namrata Kale [2] and Shiladitya Paul [1,2,*]**

[1] Materials Innovation Centre, School of Engineering, University of Leicester, Leicester LE1 7RH, UK; garima.nano@gmail.com (G.M.); ngm11@leicester.ac.uk (N.G.M.); abnj1@leicester.ac.uk (A.B.N.J.)
[2] Materials Performance and Integrity Group, TWI, Cambridge CB21 6AL, UK; david.martelo@twi.co.uk (D.M.); namrata.kale@twi.co.uk (N.K.)
* Correspondence: shiladitya.paul@twi.co.uk

**Abstract:** In recent years, there has been growing interest in thermal spray techniques using suspension or solution-based coatings. These techniques offer precise control over particle size and microstructure, improving feedstock flowability and allowing for high-quality coating customization. Spray parameters, such as stand-off distance (SOD) and feedstock flow rate, can alter the performance and characteristics of these coatings. Geothermal power plant heat exchangers often face issues like corrosion, scaling, and fouling. The literature suggests that these issues could be mitigated, at least in part, by the use of spray coatings. In this study, $TiO_2$ coatings were applied on a carbon steel substrate using suspension plasma spray (SPS) to enhance the performance of geothermal heat exchanger materials. The impact of SOD (50, 75, and 100 mm) and feedstock flow rate (10, 20, and 30 mL/min) on these coatings was examined through various techniques, including scanning electron microscope (SEM), profilometry, X-ray diffraction (XRD), and adhesion testing. The results demonstrated that coatings deposited using a 10 mL/min feedstock flow rate were well adhered to the substrate due to the efficient melting of the coating material, but as the SOD and feedstock flow rate increased due to poor thermal and kinetic energy exchange between the torch and feedstock particles, adhesion between the coating and substrate decreased.

**Keywords:** suspension plasma spray; $TiO_2$ coatings; coating microstructures; spray parameters



**Citation:** Mittal, G.; Malik, N.G.; Bhuvanendran Nair Jayakumari, A.; Martelo, D.; Kale, N.; Paul, S. Spray Parameters and Coating Microstructure Relationship in Suspension Plasma Spray $TiO_2$ Coatings. *Coatings* **2023**, *13*, 1984. https://doi.org/10.3390/coatings13121984

Academic Editor: Lech Pawlowski

Received: 10 October 2023
Revised: 17 November 2023
Accepted: 20 November 2023
Published: 22 November 2023



## 1. Introduction

Geothermal energy is a potential source of sustainable and renewable energy. However, despite having the ability to provide clean and reliable power generation, geothermal energy has yet to reach its full potential. Because the performance and durability of various components of geothermal power plants are under constant threat of corrosion and scaling due to harsh environmental conditions such as high temperature, varied pH, humidity, silica, and acids [1], these issues adversely affect the stability and efficiency of the power plant, leading to increased operation and maintenance (O&M) costs. Stainless steel and titanium are the most commonly used materials in designing geothermal plants' components. Stainless steel provides corrosion resistance, high-temperature sustainability, excellent mechanical strength, and durability. Titanium is also an excellent choice for geothermal heat exchangers due to its lightweight and outstanding corrosion resistance [2]. Material selection depends on the geothermal fluid chemistry influenced by geographical location and heat exchanger configuration. In the long term, replacing components of the heat exchanger is expensive as compared to applying paints and coatings on the geothermal plant's components. Coatings designed for geothermal power plant components, particularly geothermal heat exchangers, could offer a feasible and economical solution, providing protection against extreme thermal gradients, aggressive fluids, and mechanical stress [3,4].

For instance, F. Zhang et al. developed cermet (WC-CoCr, CrC-NiCr) and alloy (Ni self-fluxing, Fe-based amorphous) coatings using liquid feedstock-based high-velocity oxy-fuel (HVOF) for geothermal drilling components, and found negligible damage to coatings in a simulated geothermal erosion–corrosion environment [5]. Furthermore, coatings, especially surfaces with micro and/or nanostructures play a crucial role in improving the overall efficiency and reliability of geothermal energy generation [6]. Recently, F. Fanicchia et al. presented a detailed review summarizing various coatings and paints used in geothermal power plants [7]. Paints, due to their high thickness, limited stand-alone mechanical properties, and low thermal conductivity, have limited applications in geothermal environments. While coatings (or inorganic coatings), due to sustaining higher mechanical, tribological, and thermal stress than paints, are widely used in high-temperature geothermal applications. High entropy alloys (HEAs) are a new class of alloys that show promising performance in high-temperature geothermal environments due to the good corrosion performance of the CoCrFeNiMo alloy [8,9]. The thermo-mechanical and corrosion performance in a geothermal environment could be altered by adding or removing other alloying elements [10]. However, the high cost associated with HEAs restricts their potential use towards cost-efficient geothermal energy. Ceramic oxides could also be suitable candidates for geothermal applications, as they can be deposited via various coating techniques such as electroplating, thermal spray, dip coating, chemical vapor deposition, and physical vapor deposition [11,12].

Compared to other coating methods, thermal spray coatings have gained attention due to depositing high-quality coatings with tailored properties in a time- and cost-efficient manner. Thermal spray gives the freedom to deposit a wide range of coating materials on varied substrates [13,14]. Conventional powder-based thermal spray is widely accepted and employed in various industries but when it comes to depositing very small particles (<10 microns), poor injection due to low inertia of particles restricts the use of gas as a carrier. Therefore, liquid-carrying submicron particles (suspension) or a solution of chemical precursors of the coating material, forming solid particles during flight, are preferred so that coatings with nano- and micro-scale features can be obtained [15]. In addition, using liquid in the form of a suspension or solution or both provides better flowability of the feedstock as well as enhanced control over coating microstructures [16]. There is no specific microstructure that is suitable for each geothermal heat exchanger as the choice of microstructure is influenced by different factors including geothermal plant location (as the geothermal fluid chemistry and constituents vary with the location of the geothermal plant) and types of heat transfer (boilers, condensers, and evaporators). Generally, dense coatings with controlled cracking or columnar structures are preferred in geothermal environments, providing better protection against corrosive agents along with tolerance for thermal cycling. For better control over coating microstructure and properties, it is essential to understand the relationship between coating deposition/spray parameters and coating properties. The performance and characteristics of liquid feedstock-based thermal spray coatings are influenced by numerous key depositing parameters, for instance, feedstock type, feedstock flow rate, particle size, feedstock concentration, solvent type, plasma current and voltage, primary gases' type and flow rate, stand-off distance, and substrate size, shape, and temperature [17].

In this study, suspension plasma spray (SPS) was used to deposit $TiO_2$ coatings onto a carbon steel substrate. $TiO_2$ coatings were chosen to protect the geothermal heat exchangers' components against corrosion and erosion as geothermal fluids contain abrasive particles, and to provide high-temperature stability and chemical stability to geothermal heat exchanger components, protecting them against extreme heat conditions (although a corrosion and heat conductivity study is not performed in this manuscript). In addition, there are many reports available mentioning that the use of $TiO_2$ coatings in heat exchangers improves their thermal conductivity [18–20]. These coatings are formed using an aqueous suspension of $TiO_2$ nanoparticles as the feedstock material. The aqueous suspension was chosen due to cost-effectiveness, environmental considerations, safety

concerns, and avoiding waste disposal issues. The effect of stand-off distance (SOD; the distance between the injector nozzle and the substrate surface) and feedstock flow rate on the coating microstructure was focused, as it is crucial for optimizing the coating process and attaining desirable coating performance [14].

This work focuses on investigating the effect of feedstock flow rate and stand-off distance on coating microstructures in our experimental setup, which was designed to optimize energy consumption, establishing a foundational understanding. Higher power levels might generate excessive heat input, causing thermal stress or distortion in the substrate. Therefore, an SG100 plasma gun with a low power level (~32 kW) was used considering the low thickness of the prototype plate heat exchanger (0.6 mm). Also, for attaining precise and stable flow rates, a syringe pump (Teledyne ISCO® 260D; Lincoln, NE, USA) connected to the external nebulizer (constructed from a modified RS air brush AB931; Northants, UK) was used, which controlled the flow rate through a combination of motor drive mechanisms, microprocessor control, user input, feedback sensor, and advanced flow rate algorithms. Usually, a high solid content of coating material is used in suspensions. Since nanomaterials are expensive and tend to form agglomerates, making it difficult to formulate a stable and uniform suspension at a higher weight percentage of the coating nanomaterial, a low solid content was used in this study. Comprehensive analyses of coatings deposited via systematically varied SOD and the feedstock flow rate were performed using scanning electron microscopy (SEM), roughness measurements, and tape adhesion tests. The findings of this work will help in optimizing the SPS of $TiO_2$ coatings on geothermal heat exchangers, enhancing their corrosion resistance, scaling resistance, and fouling resistance.

## 2. Materials and Methods

### 2.1. Substrate Material

Coatings were developed on 25 × 25 × 6 mm coupons of carbon steel (S275JR, EN 10025-2). Prior to coating deposition, carbon steel substrates were grit blasted with #100 mesh white alumina to improve coating adhesion. The grit blasting parameters were ~551 kPa set pressure (~482 kPa run pressure) at 80 mm SOD. This process was followed by degreasing with acetone to clean the samples just before the coating deposition. The average surface roughness ($R_a$) of the substrate after grit blasting was 2.32 µm.

### 2.2. Coating Material

An aqueous suspension of 5 wt.% $TiO_2$ nanoparticles, commercially obtained from Promethean Particles Ltd. (Nottingham, UK), was used as feedstock material. Since the feedstock was a homogeneous suspension of nanoparticles, no pre-treatment was required. The particle size of $TiO_2$ in the suspension was 5–10 nm as characterized by the supplier.

### 2.3. Coating Development

Suspension plasma spraying was performed using a Praxair®SG-100 plasma gun (Praxair S.T. Inc., Indianapolis, IN, USA) attached to an OTC AII-V20 robot (OTC Daihen Inc., Tipp City, OH, USA). The APS plasma console was 3710 (Praxair S.T., Inc., Indianapolis, IN, USA) with an HF 2210 starter kit. The horizontal speed of the robot was 450 mm/s with a 5 mm vertical increase. The suspensions were fed radially into the plasma through a syringe pump (ISCO® 260D) connected to the external nebulizer (constructed from a modified RS air brush AB931). The diameter of the injector was 0.5 mm. Suspension plasma spraying (SPS) was performed at a plasma current of 700 A and voltage of 46 V. A combination of argon (49 L/min) and hydrogen (0.9 L/min) gases was used as a plasma source, and argon (3 L/min) was used as a carrier gas. The number of passes was kept constant, i.e., 50, during plasma trials. The experimental setup for spraying is shown in Figure 1 and the summary of plasma spraying is given in Table 1.

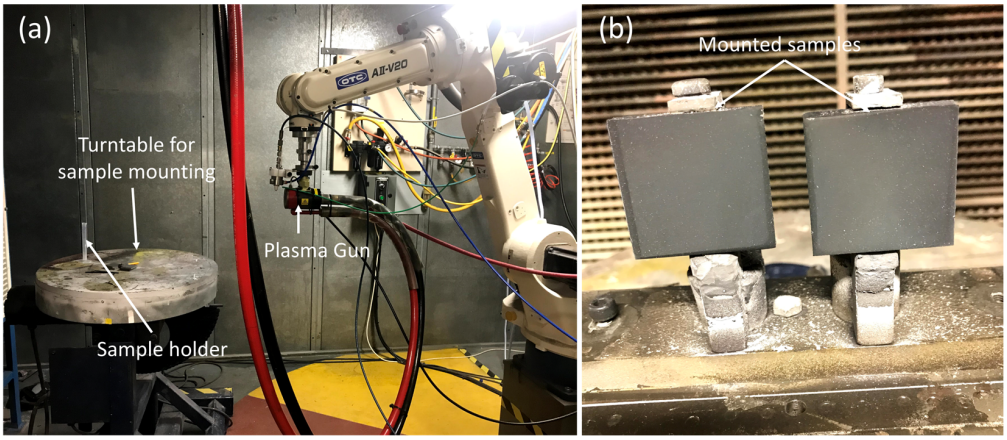


**Figure 1.** (**a**) The experimental setup for spraying and (**b**) mounted (coated) samples.

**Table 1.** Summary of suspension plasma spray parameters.

| Sample Name | Feedstock Flow Rate (mL/min) | Stand-Off Distance (mm) |
|---|---|---|
| Ti-50-10 | 10 | 50 |
| Ti-50-20 | 20 | 50 |
| Ti-50-30 | 30 | 50 |
| Ti-75-10 | 10 | 75 |
| Ti-75-20 | 20 | 75 |
| Ti-75-30 | 30 | 75 |
| Ti-100-10 | 10 | 100 |
| Ti-100-20 | 20 | 100 |
| Ti-100-30 | 30 | 100 |

### *2.4. Coating Characterisation*

The coating mass was determined by measuring the difference in weight between the sample after and before the coating application. A Sartorius CPA324S four-figure Analytical Balance (Göttingen, Germany) was employed for this weighing process. Deposition efficiency (DE), which indicates the productivity of the process for different spray conditions, was calculated based on ISO 17836:2017 [21].

An EVO LS15 SEM (Zeiss, Jena, Germany) was used to characterise the top-view morphology and the cross-section of the coated samples. An acceleration voltage of 20 kV was used at a working distance of 8.5 mm. EDX analysis of developed coatings was performed using an EDAX spectrometer, and the data were taken at 1K magnification. For cross-sectional SEM imaging, cross-sections were cut using a slow-speed precision saw and mounted in cold EpoFix resin (Buehler, Lake Bluff, IL, USA), followed by grinding (SiC papers P120, P320, P600, P1200, and P2500 from Abrasives, Brighouse, UK) and polishing (with 3 µm and 1 µm clothes). The quantitative evaluation of the porosity of deposited coatings was performed using ImageJ software (version 1.8.0; provided by the National Institutes of Health, Bethesda, MD, USA). For that, 10 images of each coating type along the cross-section were taken randomly at 1000× magnification factor. For image analysis, image filtering was applied to remove noise, followed by image segmentation by thresholding to obtain binary images. The measured pores were categorized based on three area ranges, namely 0.01–1 $\mu m^2$, 1–10 $\mu m^2$, and >10 $\mu m^2$, referring to the fine, medium, and large range pores, respectively. XRD analysis was performed to assess the phase composition of suspension plasma spray $TiO_2$ coatings, using a Bruker AXS D8 diffractometer (Billerica, MA, USA) with a Cu Kα radiation source with λ 0.1542 nm at 40 KV and 100 mA. Scans were taken from 10° to 90° 2θ range with 0.02 steps per second scan rate. The volume

percentage of the anatase phase ($C_A$) in a rutile–anatase mixture can be calculated using the following formula (Equation (1)) [22,23]:

$$C_A = \frac{8I_A}{(8I_A + 13\ I_R)} \quad (1)$$

where $I_A$ and $I_R$ are X-ray peak intensities of anatase (101) and rutile (110) phases, respectively. Also, anatase and rutile phase crystallite size was calculated from XRD data using the Scherrer equation. A non-contact 3D optical profilometer (Alicona InfinteFocus SL; Alicona Imaging GmbH, Graz, Austria) was used to characterise the surface roughness profile of the deposited specimens using a 5× objective. The analysed area was 25 mm × 25 mm for each coating. A tape adhesion test based on ASTM D3359-17 [24] was performed by cutting a 5 × 5 (at least) grid pattern of 1 × 1 mm squares into the sample surface using an Elcometer 1540 Cross Hatch Cutter (Elcometer Inc., Warren, MI, USA) to ensure that the scraped channels went through the coating and into the steel substrate beneath. Once the pattern was cut, Elcometer 99 Adhesion Test tape (Elcometer Inc.) was carefully adhered to the surface. It was then pulled off at 180° to the sample surface in a single motion, and samples were examined for material loss and delamination.

## 3. Results and Discussion

The average weight gain of all samples is presented in Figure 2a. It can be seen from the figure that the weight increased along with the increased feedstock flow rate, which can be explained by the fact that when more feedstock material is inserted into the plasma flame, after fragmentation, bigger droplets are formed, which travel in the core region of the plasma and do not deviate from the path [25]. Hence, more material is deposited on the substrate, meaning more weight gain. In the case of SOD, the weight gain fluctuates with the feedstock flow rate. At a low feedstock flow rate (10 mL/min), the weight gain decreases with the increased SOD. This could be because, at a lower feedstock flow rate, smaller droplets with less material are formed, which, after the evaporation of water, give rise to small-size agglomerates. Small droplets/particles tend to follow the gas trajectory and deviate from the central region, leading to less material deposition [25]. Simultaneously, coatings deposited at higher SOD (100 mm) with a higher flow rate (30 mL/min) show more weight gain due to the formation of larger droplets hitting the substrate.

The deposition efficiency (DE) of all samples is shown in Figure 2b, and it was found that all samples show low DE. When spraying suspension feedstock, the solvent evaporates, and only solid content reaches the substrate. It should be noted that DE is the underestimated value due to the loss of feeding material during acceleration and deceleration and overspray of the torch robot [14]. Although a larger substrate can help resolve overspray to some extent (for smaller substrate, due to being carried away with the airflow, sprayed particles tend to overshoot the edges and be lost to the surrounding environment; meanwhile, in the case of the larger substrate, a greatest distance is travelled by sprayed particles before reaching the edges, retaining more material on the substrate), the loss of feedstock material during acceleration and deceleration is unavoidable. The comparison of DEs is still valid as these accuracies are standard for each sample. Low DE is also associated with the radial injection of the feedstock material because, sometimes, the small droplets cannot reach the core region of the plasma plume. Instead, they deflect from their path, leading to insufficient energy exchange, and hence poor deposition occurs. It was observed that at a lower flow rate (10 mL/min), with the increased SOD, DE decreases. This can be elucidated by the fact that when a smaller amount of material is introduced into the plasma after fragmentation, it leads to the formation of smaller droplets. These smaller droplets may not efficiently reach the substrate as they tend to follow the gas trajectory. So, more material is deposited at a smaller SOD (50 mm), where the substrate is comparatively closer to the gun, and the kinetic energy is higher than at longer SODs (100 mm). Meanwhile, DE increases for a higher feedstock flow rate (30 mL/min) at longer SODs because, due to the

injection of more feedstock material, larger droplets are formed that have more inertia and higher kinetic energy compared to the smaller droplets. Hence, more material is deposited.

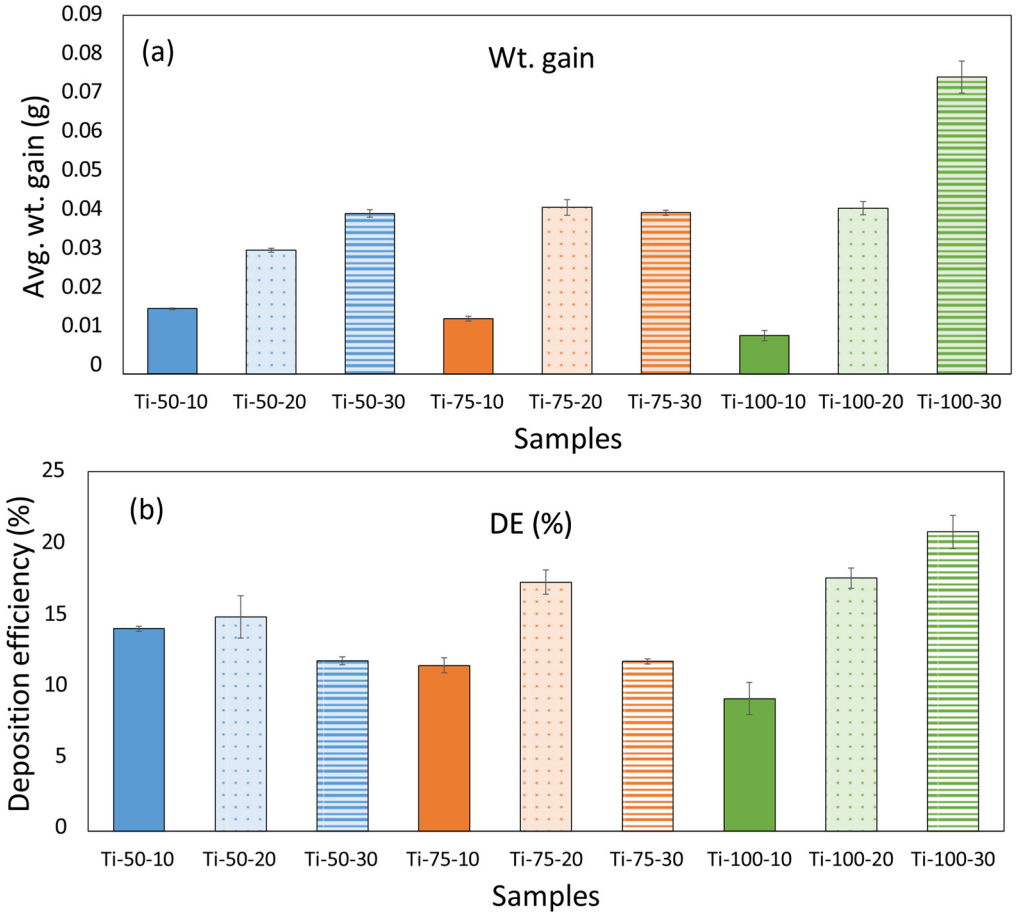


**Figure 2.** (**a**) Average weight gain and (**b**) deposition efficiency of different $TiO_2$ coatings.

The SEM images of $TiO_2$ coatings at different magnifications are shown in Figures 3 and 4. All coatings show typical cauliflower-like topography due to the deposition of feedstock material in the asperities of the substrate after hitting it at shallow angles. This phenomenon is referred to as the "shadow effect", and it becomes more pronounced when dealing with smaller droplets. These smaller droplets deviate from their intended path as they follow the gas trajectory, often depositing on substrate asperities while moving parallel to the substrate surface [25].

It was found that fully-melted and thinner splats are formed at smaller SODs (Figure 3; circle 1), while thicker splats with partially melted or re-solidified feedstock droplets (Figure 3; circle 7) take place at longer SODs. This happens because, at smaller SODs, the thermal and kinetic energy of formed droplets are higher than the longer SODs. Hence, fully melted droplets hit the substrate with a higher impact, spreading and covering the substrate properly. Meanwhile, at longer SODs, due to the insufficient thermal and kinetic energy transfer, rougher and thicker splats are formed. Also, at longer distances, nanomaterials, because of their high surface area, cool down very quickly and re-solidify even before hitting the substrate or sticking to the surface, giving rise to voids after being trapped between subsequent splats [26].

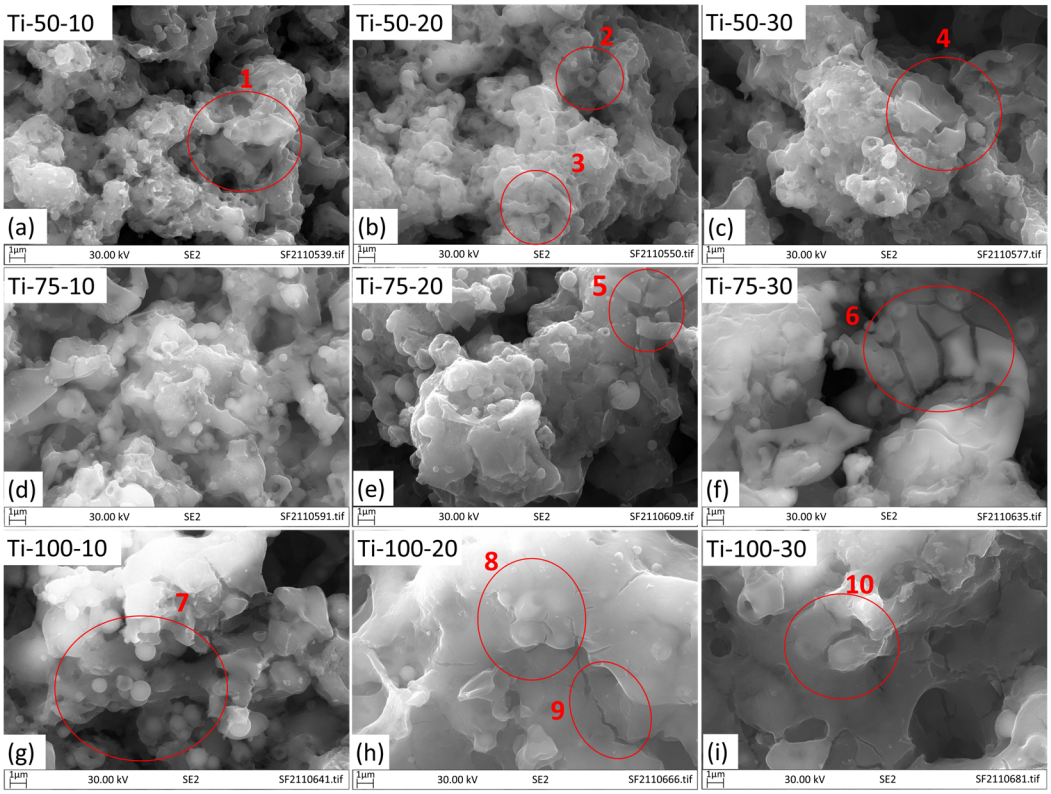


**Figure 3.** SEM images of different $TiO_2$ coatings at 1000× magnification.

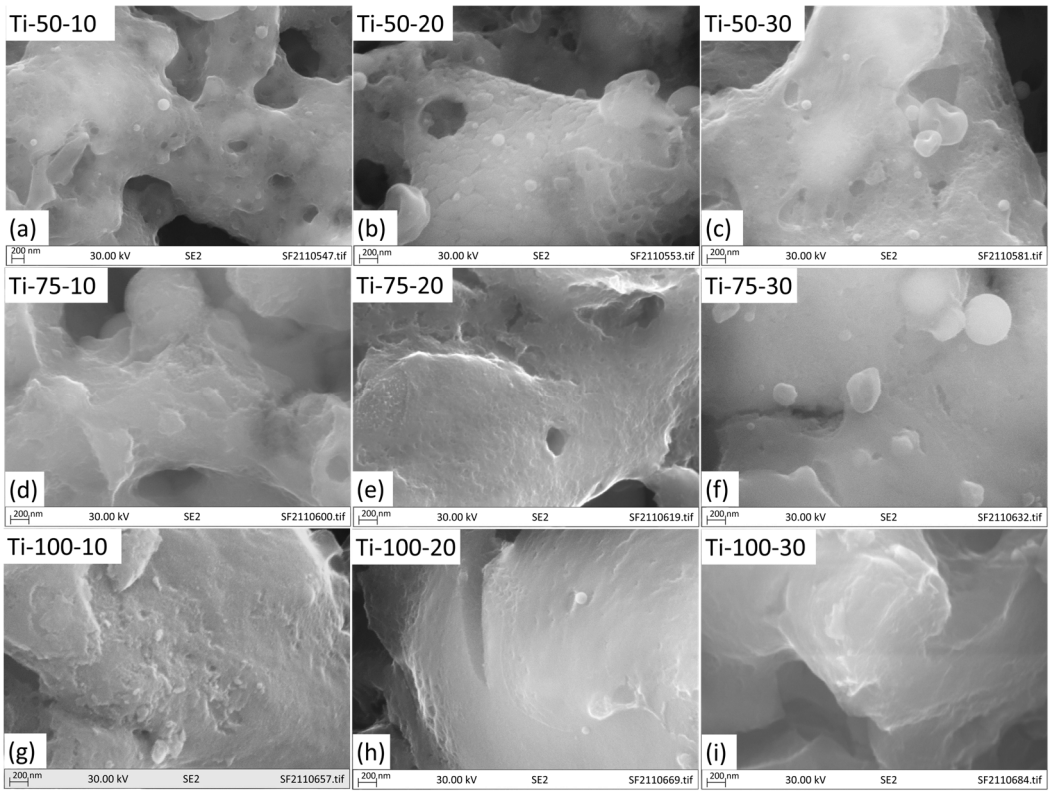


**Figure 4.** SEM images of different $TiO_2$ coatings at high magnification (10,000×).

With the increased feedstock flow rate, rougher splat formation, partial melting of feedstock droplets (Figure 3; circles 2, 3, 8 & 9), and mud-like crack formation (Figure 3;

circles 4, 5 & 6) also increase due to solvent evaporation. This can be explained by noting that when additional feedstock material is introduced, a greater volume of solvent (water) is also injected into the system. This additional solvent serves to cool down the flame. This leads to a comparatively lower heat transfer from the plasma to feedstock droplets. Hence, rougher and thicker splats and partial or no melting of $TiO_2$ droplets take place [27]. When these partially molten or unmolten particles deposit on the substrate, there is a difference in their temperature, microstructures, mechanical properties, and bonding characteristics, and the non-uniform distribution of these particles could result in localized stress concentrations, potentially generating mud-crack formation in certain parts of the coating. Figure 4 shows the splat morphology of coatings at higher magnification. As can be seen from the figure, the surface of formed splats is very smooth for coatings deposited at 50 mm SOD with a 10 mL/min feedstock flow rate. As the SOD and flow rate increases, the splat surface becomes comparatively rougher, and the presence of semi- or unmelted particles also increases.

From EDX analysis, it was found that all coatings show peaks related to elements Ti, O, Fe, and C. Also, the Fe peak intensity decreases with the increased flow rate which can be ascribed to the increased thickness of the deposited coating with the increased flow rate. For instance, the EDX pattern of coatings deposited at 75 mm SOD using 10, 20, and 30 mL/min feedstock flow rates are shown in Figure 5. Also, it was found that the coatings deposited at 100 mm SOD using a 30 mL/min feedstock flow rate exhibited high carbon content which could be possible because of the presence of surfactant (0.1%–1.0%) in the $TiO_2$ suspension. When more feedstock is injected into the plasma, due to the reduction in enthalpy, poor melting takes place (which is also evident from SEM data), implying the presence of the surfactant in the Ti-100-30 sample.

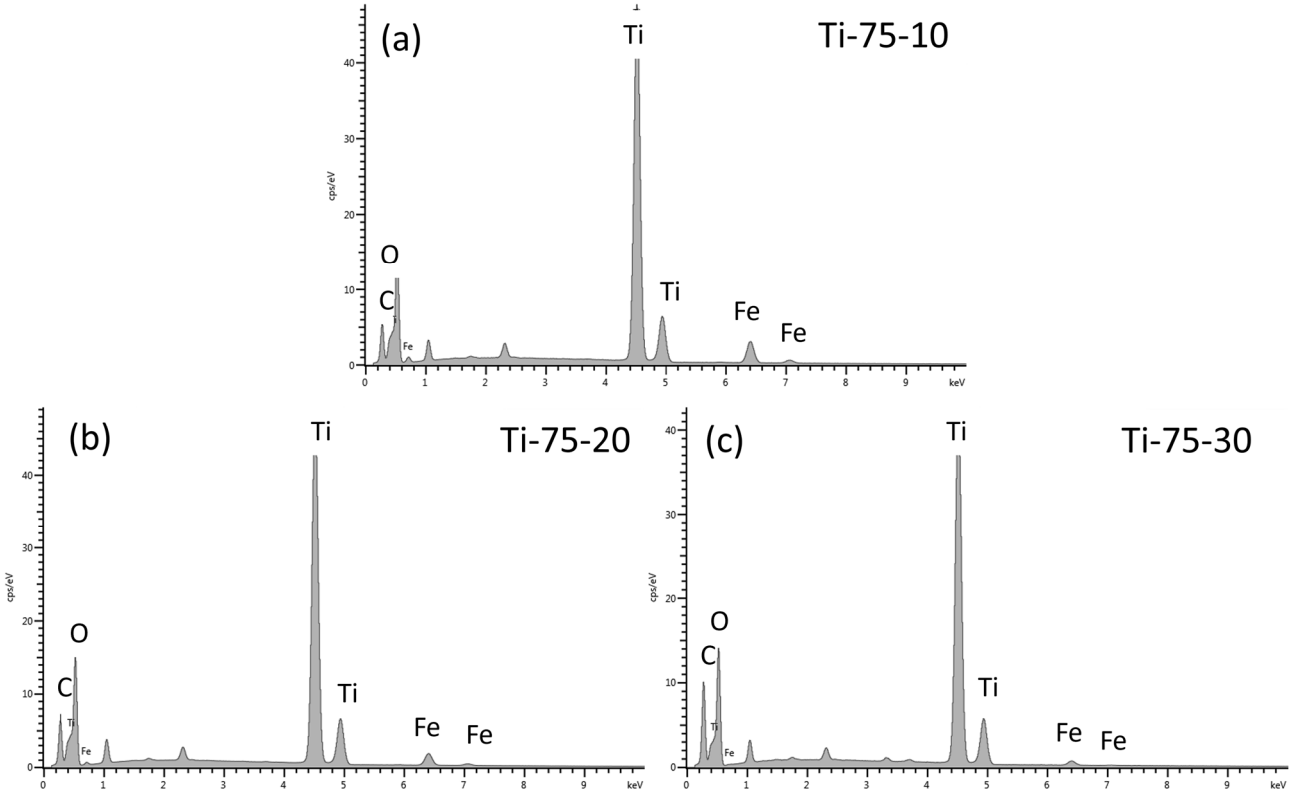


**Figure 5.** EDX pattern of $TiO_2$ coatings (**a**) Ti-75-10, (**b**) Ti-75-20, and (**c**) Ti-75-30.

Cross-sectional back-scattered SEM images of developed coatings are shown in Figure 6. Since the substrate was pre-treated with alumina grit blasting before coating deposition for better adhesion between the coating and the substrate, the formation of columnar structures

is more favourable than vertical cracks or smooth coatings [28]. This happens because when particle droplets travel toward the substrate perpendicularly, only big particles possessing a high moment of inertia hit the substrate perpendicularly. Smaller particles easily be influenced by the drag force of the plasma trajectory and deviate from their original direction, impacting the substrate at a shallow angle, and deposit on the nearest asperities, forming columnar features (shadowing effect). After subsequent deposition and vertical and horizontal growth, cone-shaped structures are developed, where inter-columnar voids separate these cones/columns, and the heads of the columns give rise to a typical cauliflower-like morphology [29].

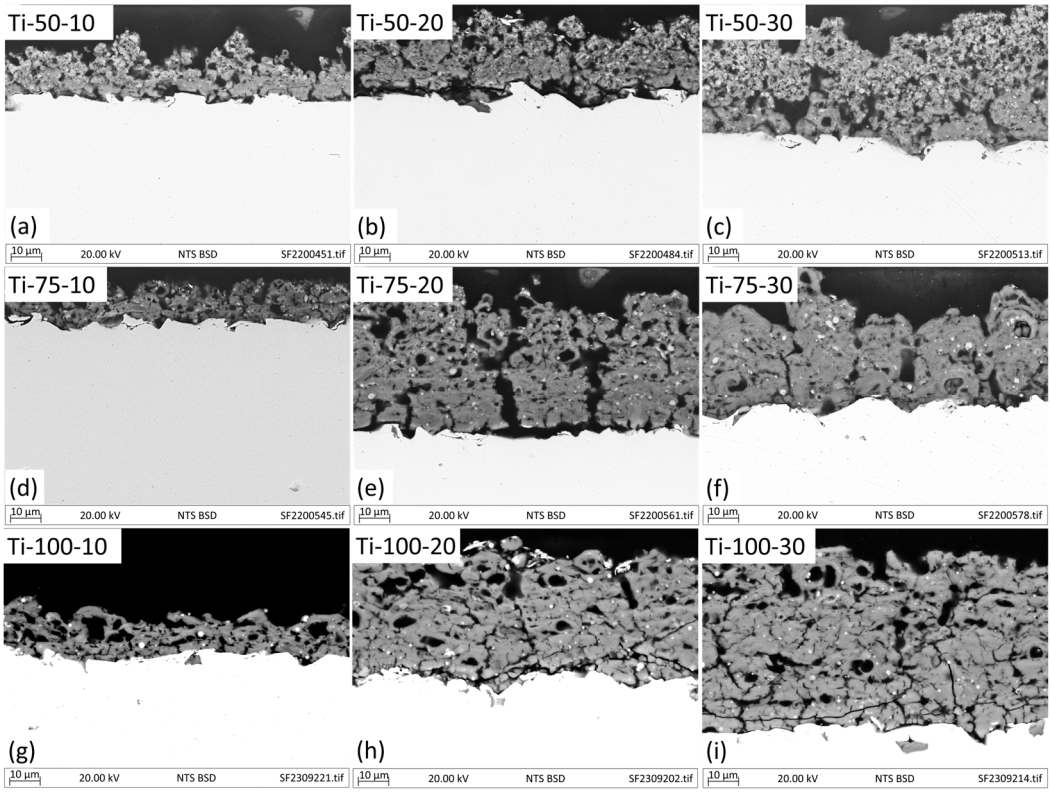


**Figure 6.** Cross-sectional back-scattered SEM images of different $TiO_2$ coatings.

Coatings deposited using 10 mL/min do not exhibit column formation prominently due to the inefficient coverage of the substrate (thinner coatings). Simultaneously, coatings deposited at 50 mm SOD show sharper peaks in cross-sections because of the high impact and kinetic energy of the particles, which hit the substrate with high accelerated force, depositing well-spread splats over the substrate's asperities. As the coating becomes thicker, column formation and their separation (inter-columnar voids) can be observed clearly (Figure 6e,f) [29]. At longer SODs, due to inefficient kinetic and thermal energy exchange, thicker splats are formed that give rise to wide and comparatively round-shaped peaks. Also, it was found that with the increased feedstock flow rate, partially melted, unmelted, and agglomerated/sintered feedstock particles were observed more prominently, leading to more porous coating with vertical crack formation (Figure 6c). The coatings at 50 mm SOD, especially deposited using 20 and 30 mL/min feedstock flow rates, exhibited the presence of more partially melted or unmelted feedstock particles and more porosity as compared to the coatings developed at 75 mm SOD and 20 and 30 mL/min feedstock flow rates (Figure 6e,f). This can be explained by the fact that at a shorter distance, feedstock droplets do not have sufficient time for solvent evaporation, agglomeration, sintering, and melting, consequently giving rise to more porous coatings [30]. Meanwhile, at longer SODs,

melted material sometimes cools down even before hitting the substrate, and rather than forming a splat, adheres to the previously deposited splats.

The porosity data are presented in Figure 7, and it was found that the total porosity area percentage for all the coatings was in a range from 23%–37%. There was no discernible trend observed based on the variations in spray parameters. In terms of different pore sizes, the percentage of fine pores was almost similar for all coatings. For coatings deposited at 75 mm, the area percentage of large pores was higher than coatings deposited at 100 mm SOD. The possible reason behind this could be that the column formation in 75 mm SOD coatings gave rise to vertical cracks which acted as large pores during image analysis. However, for 100 mm SOD coatings, the major contribution in area percentage of large pores was from the voids that developed because of poorly-/semi-molten or unmelted coating particles.

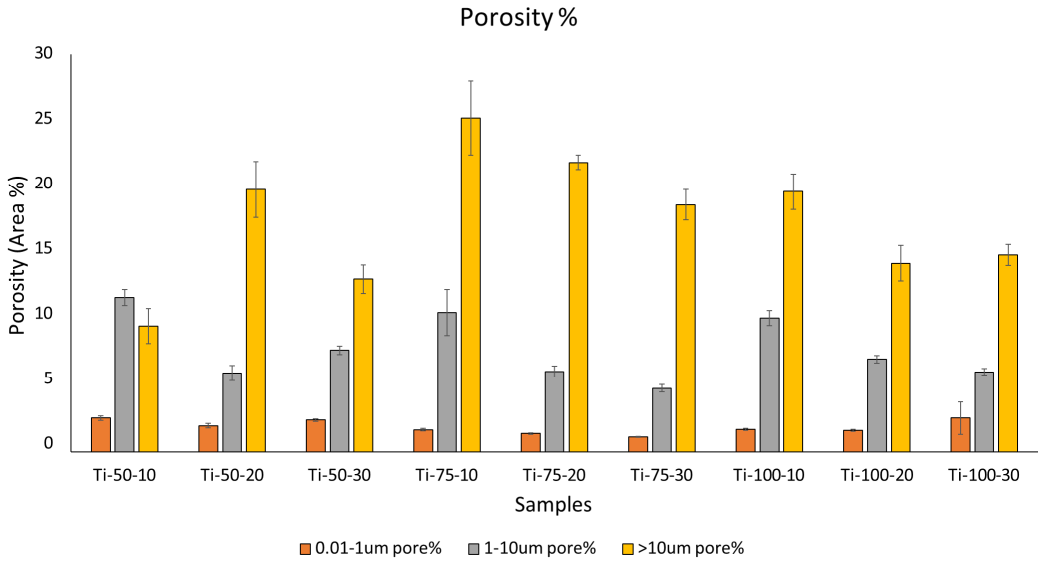


**Figure 7.** Comparison of relative pore range contribution to the total porosity of various $TiO_2$ coatings.

The spray parameters are critical in influencing the particle impact energy, coating microstructures, and coating roughness. The $R_a$ (average roughness), $R_q$ (root mean square roughness), $R_z$ (maximum height roughness), $R_{ku}$ (kurtosis: sharpness of the surface's peaks and valleys), and $R_{sk}$ (skewness: asymmetry of the surface) values are shown in Figure 8. It was found that with an increased feedstock flow rate, the $R_a$, $R_q$, $R_z$, and $R_{sk}$ increase because at a higher feedstock flow rate, particle accumulation, over-deposition, and insufficient particle flattening take place, resulting in a coating with higher porosity and rougher surface texture. With the feedstock flow rate, $R_{ku}$ was increased but only for 50 mm SOD. In comparison, for 75 mm and 100 mm SODs, $R_{ku}$ was almost similar, which means that at 50 mm SOD, due to the comparatively high impact of particles, sharper peaks and valleys are formed on the substrate's asperities. For Ti-50-20, the $R_{sk}$ value was negative, indicating that there were more valleys or depressions on the surface than peaks.

The roughness values were almost similar for the coatings deposited at different SODs using a low feedstock flow rate, i.e., 10 mL/min. In comparison, this trend changes at higher 20 and 30 mL/min, resulting in a decreased roughness with the increased SOD. This can be elucidated by the fact that, at lower feedstock flow rates, the formation of flattened splats with extensive substrate coverage occurs. This results in a well-adhered coating due to the adequate melting of the coating material. Also, it can be concluded that at higher SODs, the sharpness of peaks/columns decreases because the insufficient kinetic and thermal energy exchange gives rise to thicker (disc-like) splats, forming columns with globular heads after subsequent deposition [31,32].

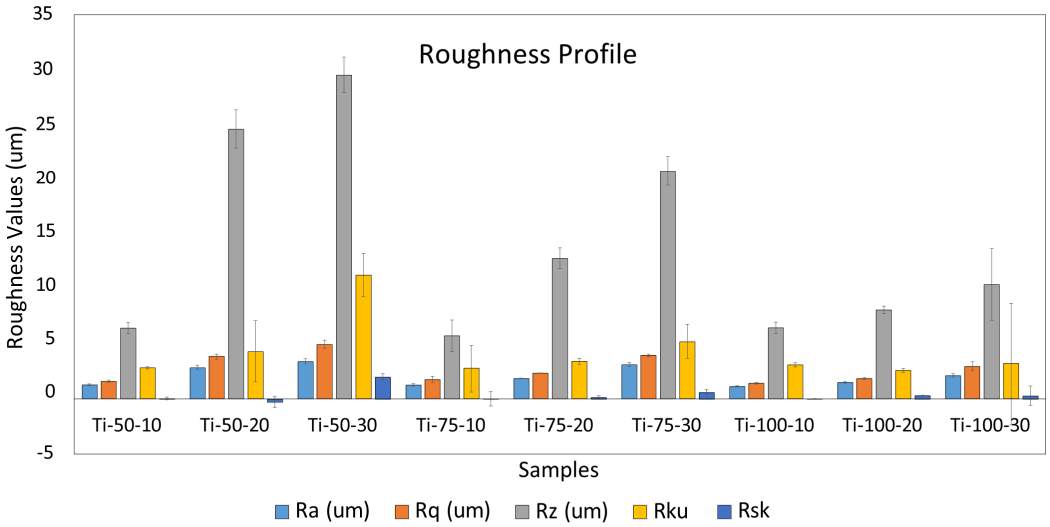


**Figure 8.** Roughness profile of different $TiO_2$ coatings.

The crystalline structure of $TiO_2$ coatings deposited at different spray conditions was analysed by comparing XRD data, shown in Figure 9. All coatings were found to show two main phases of $TiO_2$, i.e., anatase (PDF ID: 03-065-5714) and rutile (PDF ID: 01-089-0555), and characteristic peaks related to the substrate. The peak intensity was highest for the coatings developed using a low feedstock flow rate because of low coating thickness. As the feedstock flow rate increases, the peak intensity of the substrate's characteristic peaks decreases. Various spray parameters, including SOD and feedstock flow rate, affect the phase formation and crystallite size of SPS coatings [18–20]. The crystallite size of coatings was calculated using the Scherrer equation applied to anatase (101) and rutile (110) peaks (Table 2). Regarding the anatase crystallite size, a reduction was noted with higher feedstock flow rates and a decrease in stand-off distance (SOD). This can be clarified by understanding that at longer spray distances, there is more time in-flight before reaching the substrate. This extended travel favours the formation of larger agglomerates, allowing for sufficient sintering of the material and leading to an increase in crystallite size [33]. At a higher feedstock flow rate, insufficient sintering or re-solidification due to the insertion of more solvent and reduced flame enthalpy leads to reduced crystallite size. For the rutile phase, it was observed that coatings deposited using 20 mL/min exhibited larger crystallites. The possible explanation behind this could be that at 20 mL/min, more solid content is present in the droplets, which, after efficient melting, agglomeration, and sintering, form larger crystallites as compared to the coatings deposited using 30 mL/min, where comparatively insufficient melting occurs. Although no significant difference was observed in the anatase content of all deposited coatings, a slight increase was found in the anatase content with the increased SOD (Table 2). With the increased SOD, agglomerates have more time to re-solidify during flight, forming anatase phase proportions due to homogeneous nucleation. At the same time, agglomerates that solidify on the substrate (in the case of shorter SODs) can form anatase or rutile phases depending on various factors, including agglomerate size. Usually, for agglomerates solidifying on the substrate, rutile phase formation is favoured due to the lower Gibbs free energy. However, if the agglomerate size is in the submicron range, metastable anatase phase formation takes place due to the fast solidification, suppressing the heterogeneous nucleation [33–35].

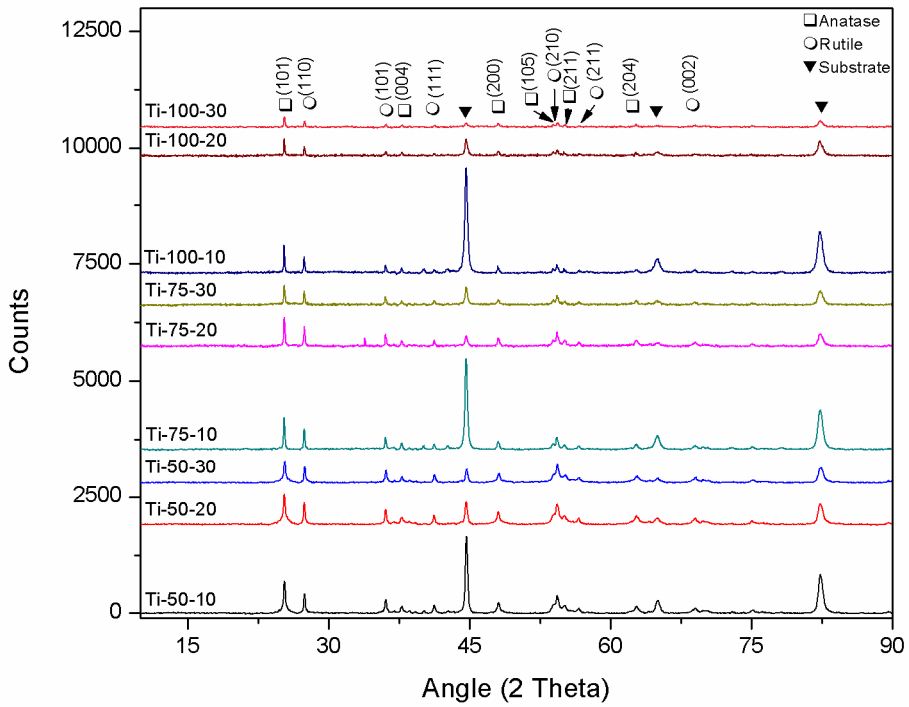


**Figure 9.** Comparison of XRD pattern of different $TiO_2$ coatings developed at varied SODs and feedstock flow rates.

**Table 2.** Comparison of volume percentage of anatase phase and anatase and rutile phase crystallite size of different $TiO_2$ coatings developed at varied SOD and feedstock flow rate.

| Sample | Anatase Content ($C_A$); % | Crystallite Size (nm) | |
|---|---|---|---|
| | | Anatase | Rutile |
| Ti-50-10 | 48 | 24.15 | 31.94 |
| Ti-50-20 | 41 | 17.2 | 36.57 |
| Ti-50-30 | 42 | 18.03 | 29.25 |
| Ti-75-10 | 47 | 44.99 | 45.29 |
| Ti-75-20 | 45 | 37.62 | 91.33 |
| Ti-75-30 | 44 | 33.96 | 48.19 |
| Ti-100-10 | 50 | 67.06 | 52.83 |
| Ti-100-20 | 45 | 50.99 | 136.95 |
| Ti-100-30 | 43 | 36.86 | 71.28 |

The macrographs of different coatings after performing tape adhesion tests (shown in Figure 10) show that the coatings deposited at a lower SOD, i.e., 50 mm, were well adhered to the substrate due to high impact and comparatively better thermal energy transfer at low SODs between the torch and feedstock particles. Also, coatings deposited using a low feedstock flow rate, i.e., 10 mL/min, showed good adhesion. When higher feedstock flow rates are used, along with more material, more solvent (water) is introduced, hence improper melting of particles due to cooling down of the plasma flame [14]. Therefore, Ti-75-20, Ti-75-30, Ti-100-20, and Ti-100-30 showed a high degree of delamination compared to others.

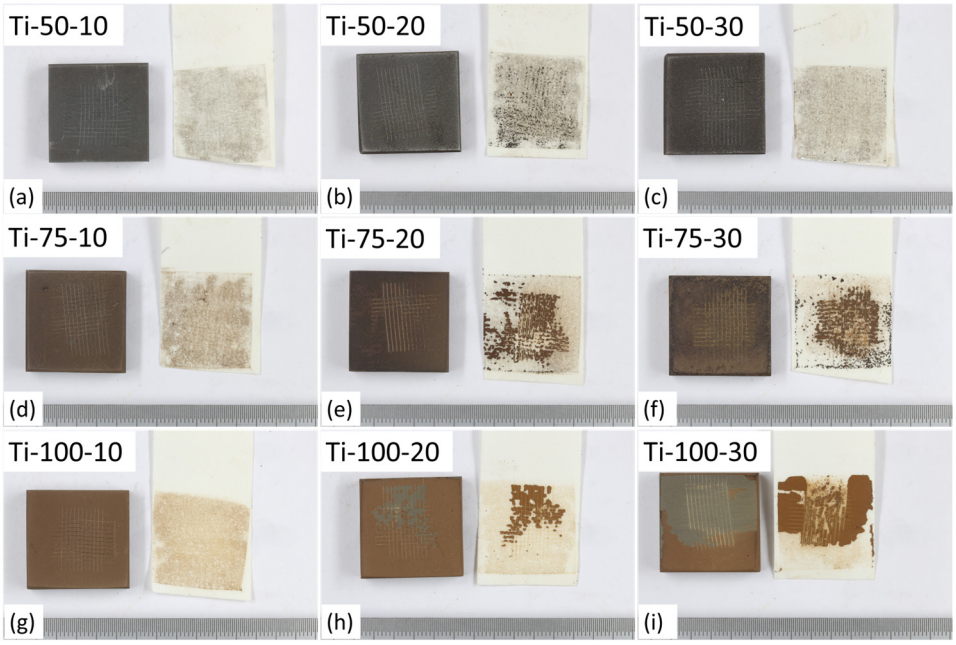


**Figure 10.** Macrographs of different $TiO_2$ coatings after tape adhesion tests.

## 4. Summary and Conclusions

Coatings with superior performance help extend the lifetime of geothermal heat exchangers and improve the overall efficiency of geothermal power plants. Thermal spray $TiO_2$ coating could be an option to protect the components of geothermal heat exchangers from corrosion and scaling. In this study, $TiO_2$ coatings were deposited through suspension plasma spray using a uniform aqueous suspension of 5 wt.% $TiO_2$ nanoparticles on carbon steel (S275JR, EN 10025-2) substrates. To understand the role of different spray parameters in coating microstructure formation, the coatings were deposited at different stand-off distances using different feedstock flow rates. It was found that at a small SOD, due to the proximity with the plasma torch, coating particles possessed high thermal and kinetic energy, which led to well-melted and smooth splat formation, hence, compact coatings. However, as the feedstock flow rate increased at a small SOD, poor melting of particles due to cooling of plasma plume, excessive material insertion, and insufficient time took place, and hence porous coatings were formed. At larger SODs, due to the poor thermal and kinetic energy exchange between the torch and feedstock particles, resolidification of feedstock particles occurred and gave rise to porous coatings. The tape adhesion tests showed that coatings deposited at 50 mm SOD (Ti-50-10, Ti-50-20 and Ti-50-30) and coatings deposited using a 10 mL/min feedstock flow rate (Ti-75-10 and Ti-100-10) were well adhered to the substrate in comparison to the coatings deposited using higher feedstock flow rates and at longer SODs (Ti-75-20, Ti-75-30, Ti-100-20, and Ti-100-30). The outcomes of this work offer a platform for further optimization and development of protective coatings for geothermal heat exchangers.

**Author Contributions:** Conceptualization, S.P.; methodology, S.P. and G.M.; investigation, G.M. and N.G.M.; formal analysis, G.M.; writing—original draft preparation, G.M. and A.B.N.J.; writing—review and editing, S.P.; supervision, S.P. and D.M.; project administration, D.M. and N.K. All authors have read and agreed to the published version of the manuscript.

**Funding:** This project has received funding from the European Union's Horizon 2020 research and innovation programme under the project: GeoHex-advanced material for cost-efficient and enhanced heat exchange performance for geothermal application (Grant agreement 851917).

**Institutional Review Board Statement:** Not applicable.

**Informed Consent Statement:** Not applicable.

**Data Availability Statement:** Data are contained within the article.

**Acknowledgments:** We want to acknowledge the contribution of the GeoHex consortium to this project.

**Conflicts of Interest:** The authors declare no conflict of interest.

## References

1. Nogara, J.; Zarrouk, S.J. Corrosion in geothermal environment: Part 1: Fluids and their impact. *Renew. Sustain. Energy Rev.* **2018**, *82*, 1333–1346. [CrossRef]
2. Benea, L.; Bounegru, I.; Forray, A.; Axente, E.R.; Buruiana, D.L. Preclinical EIS Study of the Inflammatory Response Evolution of Pure Titanium Implant in Hank's Biological Solution. *Molecules* **2023**, *28*, 4837. [CrossRef] [PubMed]
3. Nakashima, Y.; Umehara, N.; Kousaka, H.; Tokoroyama, T.; Murashima, M.; Mori, D. Carbon-based coatings for suppression of silica adhesion in geothermal power generation. *Tribol. Int.* **2023**, *177*, 107956. [CrossRef]
4. Cadelano, G.; Bortolin, A.; Ferrarini, G.; Bison, P.; Dalla Santa, G.; Di Sipio, E.; Bernardi, A.; Galgaro, A. Evaluation of the Effect of Anti-Corrosion Coatings on the Thermal Resistance of Ground Heat Exchangers for Shallow Geothermal Applications. *Energies* **2021**, *14*, 2586. [CrossRef]
5. Zhang, F.; Tabecki, A.; Bennett, M.; Begg, H.; Lionetti, S.; Paul, S. Feasibility Study of High-Velocity Oxy-fuel (HVOF) Sprayed Cermet and Alloy Coatings for Geothermal Applications. *J. Therm. Spray Technol.* **2023**, *32*, 339–351. [CrossRef]
6. Kim, D.E.; Yu, D.I.; Jerng, D.W.; Kim, M.H.; Ahn, H.S. Review of boiling heat transfer enhancement on micro/nanostructured surfaces. *Exp. Therm. Fluid Sci.* **2015**, *66*, 173–196. [CrossRef]
7. Fanicchia, F.; Karlsdottir, S.N. Research and Development on Coatings and Paints for Geothermal Environments: A Review. *Adv. Mater. Technol.* **2023**, *8*, 2202031. [CrossRef]
8. Oppong Boakye, G.; Straume, E.O.; Gunnarsson, B.G.; Kovalov, D.; Karlsdottir, S.N. Corrosion behaviour of HVOF developed Mo-based high entropy alloy coating and selected hard coatings for high temperature geothermal applications. *Mater. Des.* **2023**, *235*, 112431. [CrossRef]
9. Kumar, M.; Upadhyaya, R. Corrosion and wear analysis of HVOLF sprayed WC-10CO-4Cr coating on geothermal turbine blade. *World J. Eng.* **2019**, *16*, 768–774. [CrossRef]
10. Thorhallsson, A.I.; Fanicchia, F.; Davison, E.; Paul, S.; Davidsdottir, S.; Olafsson, D.I. Erosion and Corrosion Resistance Performance of Laser Metal Deposited High-Entropy Alloy Coatings at Hellisheidi Geothermal Site. *Materials* **2021**, *14*, 3071. [CrossRef]
11. Jayakumari, A.B.N.; Malik, N.G.; Mittal, G.; Martelo, D.; Kale, N.; Paul, S. Coatings for Geothermal Heat Exchangers. *Preprints* **2023**. [CrossRef]
12. Cai, Y.; Quan, X.; Li, G.; Gao, N. Anticorrosion and Scale Behaviors of Nanostructured $ZrO_2$–$TiO_2$ Coatings in Simulated Geothermal Water. *Ind. Eng. Chem. Res.* **2016**, *55*, 11480–11494. [CrossRef]
13. Mahu, G.; Munteanu, C.; Istrate, B.; Benchea, M.; Lupescu, S. Influence of $Al_2O_3$-13$TiO_2$ powder on a C45 steel using atmospheric plasma spray process. *IOP Conf. Ser. Mater. Sci. Eng.* **2018**, *444*, 032010. [CrossRef]
14. Mittal, G.; Paul, S. Suspension and Solution Precursor Plasma and HVOF Spray: A Review. *J. Therm. Spray Tech.* **2022**, *31*, 1443–1475. [CrossRef]
15. Fauchais, P.; Vardelle, M.; Vardelle, A.; Goutier, S. What Do We Know, What are the Current Limitations of Suspension Plasma Spraying? *J. Therm. Spray Technol.* **2015**, *24*, 1120–1129. [CrossRef]
16. Tejero-Martin, D.; Rezvani Rad, M.; McDonald, A.; Hussain, T. Beyond Traditional Coatings: A Review on Thermal-Sprayed Functional and Smart Coatings. *J. Therm. Spray Technol.* **2019**, *28*, 598–644. [CrossRef]
17. Chen, X.; Kuroda, S.; Ohnuki, T.; Araki, H.; Watanabe, M.; Sakka, Y. Effects of Processing Parameters on the Deposition of Yttria Partially Stabilized Zirconia Coating During Suspension Plasma Spray. *J. Am. Ceram. Soc.* **2016**, *99*, 3546–3555. [CrossRef]
18. Zhang, X.; Wang, Y.; Zhao, D.; Guo, J. Improved thermal performance of heat exchanger with $TiO_2$ nanoparticles coated on the surfaces. *Appl. Therm. Eng.* **2017**, *112*, 1153–1162. [CrossRef]
19. Yan, W.; Lin-lin, W.; Ming-yan, L. Antifouling and enhancing pool boiling by $TiO_2$ coating surface in nanometer scale thickness. *AIChE J.* **2007**, *53*, 3062–3076. [CrossRef]
20. Wang, L.L.; Liu, M.Y. Pool boiling fouling and corrosion properties on liquid-phase-deposition $TiO_2$ coatings with copper substrate. *AIChE J.* **2011**, *57*, 1710–1718. [CrossRef]
21. *ISO 17836:2017*; Thermal Spraying Determination of the Deposition Efficiency for Thermal Spraying. ISO: Geneva, Switzerland, 2017. Available online: https://www.iso.org/standard/69754.html (accessed on 30 August 2023).
22. Berger-Keller, N.; Bertrand, G.; Filiatre, C.; Meunier, C.; Coddet, C. Microstructure of plasma-sprayed titania coatings deposited from spray-dried powder. *Surf. Coat. Technol.* **2003**, *168*, 281–290. [CrossRef]
23. Toma, F.-L.; Sokolov, D.; Bertrand, G.; Klein, D.; Coddet, C.; Meunier, C. Comparison of the photocatalytic behavior of $TiO_2$ coatings elaborated by different thermal spraying processes. *J. Therm. Spray Technol.* **2006**, *15*, 576–581. [CrossRef]
24. Standard Test Methods for Rating Adhesion by Tape Test. Available online: https://www.astm.org/d3359-17.html (accessed on 30 August 2023).
25. Mauer, G.; Vaßen, R. Coatings with Columnar Microstructures for Thermal Barrier Applications. *Adv. Eng. Mater.* **2020**, *22*, 1900988. [CrossRef]

26. Du, L.; Coyle, T.W.; Chien, K.; Pershin, L.; Li, T.; Golozar, M. Titanium Dioxide Coating Prepared by Use of a Suspension-Solution Plasma-Spray Process. *J. Therm. Spray Technol.* **2015**, *24*, 915–924. [CrossRef]
27. Rampon, R.; Marchand, O.; Filiatre, C.; Bertrand, G. Influence of suspension characteristics on coatings microstructure obtained by suspension plasma spraying. *Surf. Coat. Technol.* **2008**, *202*, 4337–4342. [CrossRef]
28. Caio, F.; Moreau, C. Influence of Substrate Shape and Roughness on Coating Microstructure in Suspension Plasma Spray. *Coatings* **2019**, *9*, 746. [CrossRef]
29. Bernard, B.; Bianchi, L.; Malié, A.; Joulia, A.; Rémy, B. Columnar suspension plasma sprayed coating microstructural control for thermal barrier coating application. *J. Eur. Ceram. Soc.* **2016**, *36*, 1081–1089. [CrossRef]
30. Joulia, A.; Duarte, W.; Goutier, S.; Vardelle, M.; Vardelle, A.; Rossignol, S. Tailoring the Spray Conditions for Suspension Plasma Spraying. *J. Therm. Spray Technol.* **2015**, *24*, 24–29. [CrossRef]
31. Sokołowski, P.; Kozerski, S.; Pawłowski, L.; Ambroziak, A. The key process parameters influencing formation of columnar microstructure in suspension plasma sprayed zirconia coatings. *Surf. Coat. Technol.* **2014**, *260*, 97–106. [CrossRef]
32. Sokołowski, P.; Pawłowski, L.; Dietrich, D.; Lampke, T.; Jech, D. Advanced Microscopic Study of Suspension Plasma-Sprayed Zirconia Coatings with Different Microstructures. *J. Therm. Spray Technol.* **2016**, *25*, 94–104. [CrossRef]
33. Robinson, B.W.; Tighe, C.J.; Gruar, R.I.; Mills, A.; Parkin, I.P.; Tabecki, A.K.; de Villiers Lovelock, H.L.; Darr, J.A. Suspension plasma sprayed coatings using dilute hydrothermally produced titania feedstocks for photocatalytic applications. *J. Mater. Chem. A* **2015**, *3*, 12680–12689. [CrossRef]
34. Alebrahim, E.; Tarasi, F.; Rahaman, M.S.; Dolatabadi, A.; Moreau, C. Fabrication of titanium dioxide filtration membrane using suspension plasma spray process. *Surf. Coat. Technol.* **2019**, *378*, 124927. [CrossRef]
35. Bemporad, E.; Bolelli, G.; Cannillo, V.; De Felicis, D.; Gadow, R.; Killinger, A.; Lusvarghi, L.; Rauch, J.; Sebastiani, M. Structural characterisation of High Velocity Suspension Flame Sprayed (HVSFS) $TiO_2$ coatings. *Surf. Coat. Technol.* **2010**, *204*, 3902–3910. [CrossRef]